MOX–Report No. 05/2013

Simulation of oxygen transfer in stented arteries and correlation with in-stent restenosis

Caputo, M.; Chiastra, C.; Cianciolo, C.; Cutri , E.;
Dubini, G.; Gunn, J.; Keller, B.; Zunino, P.;

MOX, Dipartimento di Matematica "F. Brioschi"
Politecnico di Milano, Via Bonardi 9 - 20133 Milano (Italy)

mox@mate.polimi.it http://mox.polimi.it

Simulation of oxygen transfer in stented arteries and correlation with in-stent restenosis[†]

M. Caputo[1], C. Chiastra[1], C. Cianciolo[1], E. Cutrì[1,2], G. Dubini[1], J. Gunn[3], B. Keller[1], F. Migliavacca[1], P. Zunino[2,4]

February 10, 2013

[1] LaBS, Chemical Engineering Department "Giulio Natta", Politecnico di Milano, Italy

[2] MOX, Department of Mathematics "Francesco Brioschi", Politecnico di Milano, Italy

[3] Department of Cardiovascular Science, University of Sheffield, Sheffield, UK

[4] Department of Mechanical Engineering and Materials Science, University of Pittsburgh, Pittsburgh, PA, USA

Abstract

Computational models are used to study the combined effect of biomechanical and biochemical factors on coronary in-stent restenosis, which is a post-operative remodeling and regrowth of the stented artery tissue. More precisely, we address numerical simulations based on Navier-Stokes and mass transport equations to study the role of perturbed wall shear stresses and reduced oxygen concentration in a geometrical model reconstructed from a real porcine artery treated with a stent. Joining *in vivo* and *in silico* tools of investigation has multiple benefits in this case. On one hand, the geometry of the arterial wall and of the stent closely correspond to a real implanted configuration. On the other hand, the inspection of histological tissue samples informs us on the location and intensity of in-stent restenosis. As a result of that, we are able to correlate geometrical factors, such as the axial variation of the artery diameter and its curvature, the numerical quantification of biochemical stimuli, such as wall shear stresses, and the availability of oxygen to the inner layers of the artery, with the appearance of in-stent restenosis. This study shows that the perturbation of the vessel curvature could induce hemodynamic conditions that stimulate an undesired arterial remodeling.

1 Introduction

The correlation of disturbed flow with abnormal biological responses is a well accepted theory [15, 10]. More specifically, low flow and flow reversal on the near-wall regions induce deleterious wall shear stresses (WSS) which are hypothesized to aggravate the underlying tissue recovery [4]. The clinical placement of a stent for occlusive arterial disease has introduced new theories regarding the involvement of flow, as the major drawback to the device is the re-appearance of tissue in the stented region, known as in-stent restenosis (ISR). While the introduction of hypoxia as an agent of disease initiation is not a new theory [20], recent indications of the correlation between ISR and hypoxia have been elucidated through *in vivo* [35, 36], and *in*

[2]This work has been partially supported by the ERC Advanced Grant N.227058 MATHCARD and by the Project MeDDiCA Marie Curie Initial Training Network, EU-FP7/2007-2013 under grant agreement PITN-GA-2009-238113. Authors are listed in alphabetical order.

silico [12] studies. In fact, the inner curvature regions of the stented model within the study by [12] were subject to a lower oxygen flux; these regions correspond to the geometry-modified distribution of WSS [11]. The straightened effect of the geometry has been indicated as a means for computational fluid dynamics to identify the risk zones capable of forming ISR [22]. However, there is a lack of studies which show paired histology to the computational results. In this study, the real stent geometry obtained from a porcine coronary model was used in the construction of a fluid-wall model domain for computational fluid dynamics (CFD) and oxygen mass transport analysis [33, 32].

As the prior studies did not have actual histological data but rather an ideal domain, the use of a micro-Computed Tomography (micro-CT) rendered stent for the reconstruction of the curved coronary flow domain, may allow further insight into the interaction of physiological mass transfer of oxygen along the arterial wall in the immediate post-implant conditions.

The aim of this work is then twofold. On one hand we use computational methods to analyze and compare multiple factors that may affect ISR, such as wall shear stresses (WSS) and the availability of oxygen into the wall of the artery. Since this study deals with coronary arteries, a sensitivity study with respect to the vessel curvature is also performed. On the other hand, we compare these indicators with the observations of neointimal hyperplasia obtained from the animal model, in an attempt to infer guidelines on how the combination of biomechanical and biochemical factors affect this post-operative pathology.

2 Materials and methods

2.1 Animal studies

The volumetric geometry of a stainless steel, balloon-expandable stent (Biocompatibles Ltd., Farnham, UK) that was implanted into a healthy porcine coronary artery is considered in this study. The experimental protocol has been previously reported [27]. In brief, the stent was deployed into the healthy right coronary artery (RCA), using a balloon-to-artery ratio of 1.4:1, to induce sufficient injury for neointimal growth, yet without causing tissue laceration. The stent under investigation was harvested at 14 days, imaged with high resolution micro-CT (Skyscan, Kontich, Belgium), and reconstructed into a 3D surface mesh. Following micro-CT, the stented vessel was embedded, sectioned and submitted for histology, see Figure 1.

2.2 Geometrical models of stented arteries

To perform fluid dynamics simulations on the deformed state of the stented artery, the structural configuration of the stent and vessel surface was created using the previously established explicit method defined in [27]. A full structural model (2.8 mm internal angiographic diameter, 36 mm centerline length, and 0.1 mm wall thickness) was created using ABAQUS Explicit (v6.10, Dassault Systemes Simulia Corp., Providence, RI, USA), whereby the vessel wall was defined with hyperelastic isotropic material property prescribed by a reduced six-degrees polynomial strain energy density function [18]. The wall thickness was justified based on the notion that the ratio of wall thickness (h) to vessel diameter ($2r$) is fairly consistent ($h/2r = 0.04$) amongst all vessels [30]. The wall structure was expanded under displacement controls and then relaxed onto the stent surface with a pressure over-closure method, in order to obtain a geometry similar to immediate post-implant conditions.

Two additional geometries are addressed here, which incorporate the physiological radius of curvature, see Figure 2; this included a 36 and 20 mm curvature radii, respectively labelled as CU36 and CU20 in what follows. These values were found reasonable within measurements

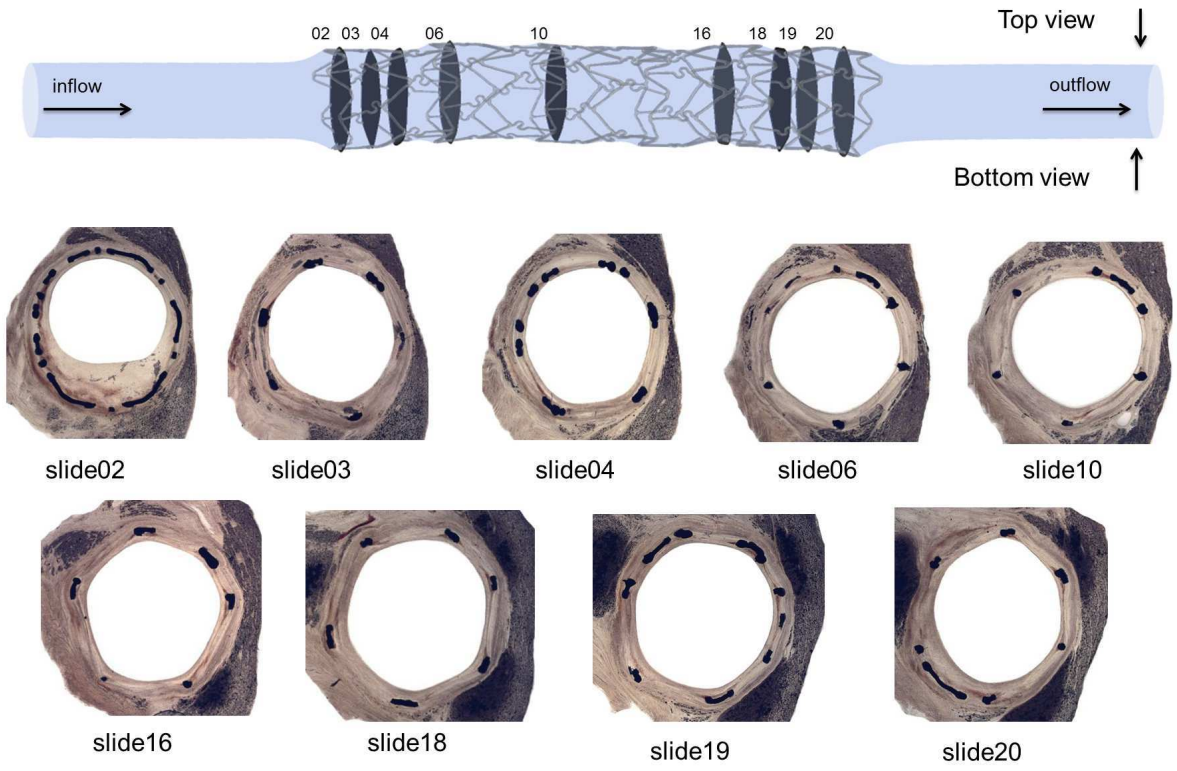

Figure 1: Histologies of the harvested artery at different locations labeled on top. To clarify the forthcoming discussion, the *top* and *bottom* views of the interface between the lumen and the arterial wall are shown. For the curved models, these views correspond to the *outer* and *inner* sides of the artery with respect to the center of curvature. In those cases, the centerline of the vessel is a curve laying on the plane of the page.

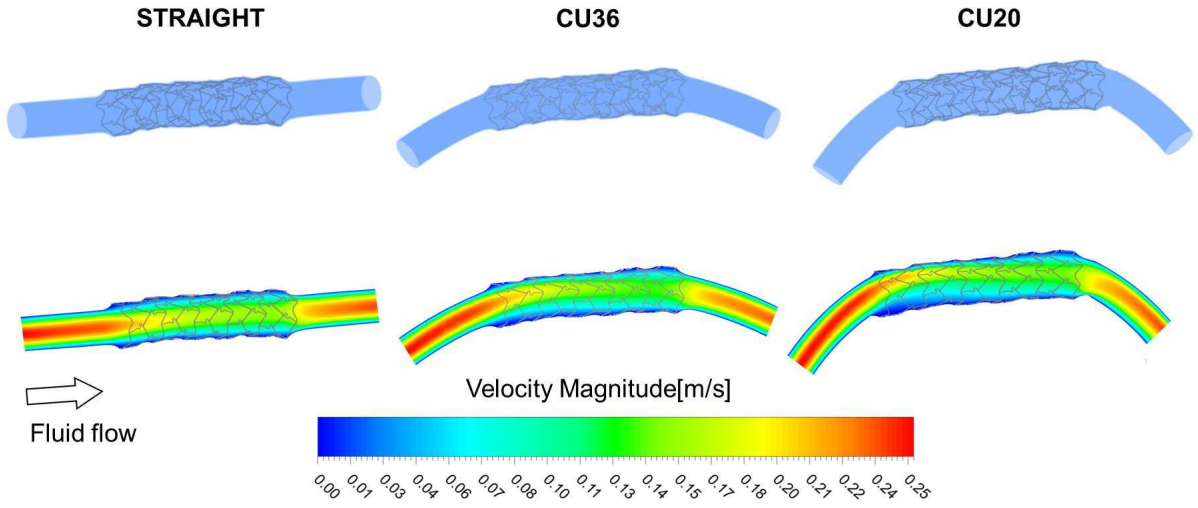

Figure 2: Top: lumen, arterial wall and stent geometry for the (a) straight, (b) CU36 (36 mm radius of curvature), and (c) CU20 (20 mm radius of curvature). Bottom: velocity magnitude contour plot for each model. As the curvature increases the velocity peak is shifted towards the outer surface of the wall (with respect to the center of curvature).

taken from 2D qualitative coronary angiographic images of similar porcine models. The centerline of the vessel is assumed to be a plane curve, positioned according to a visible residual curvature in the micro-CT images. The inlet to curvature radius ratio, defined as $\delta = r/R$ where r is the radius of the vessel and R the radius of curvature, is $\delta = 0.07$ for CU20 and $\delta = 0.04$ for CU36.

The surface domains of the internal and external artery wall and the stent are exported in the meshing software ANSYS ICEM CFD v.13.0 (Ansys Inc., Canonsburg, PA, USA) in stereolithography (STL) format [26]. A tetrahedral mesh is generated, identifying the fluid domain and the wall domain. To accomplish this task the Octree mesh method is used: it ensures refinement of the mesh where necessary, but maintains larger elements where possible, allowing for faster computation. Once the *root* tetrahedron, which encloses the entire geometry, has been initialized, this algorithm subdivides the root tetrahedron until all element size requirements are met [8]. Conformal nodes are created at the interface between the fluid domain and the vessel wall.

2.3 Governing equations for fluid dynamics and mass transfer

Navier-Stokes equations represent a well accepted model for blood flow in medium/small sized arteries [16]. When coupled with transfer and absorption of mass into the arterial walls, the pulsatile nature of blood flow is often neglected [41, 14]. As a result of that, we refer to the steady momentum and continuity equations, given as:

$$\nabla \cdot \mathbf{u} = 0, \quad \rho(\mathbf{u}\cdot\nabla)\mathbf{u} + \nabla p - \mu\Delta\mathbf{u} = 0, \quad \forall \mathbf{x} \in \Omega_l$$

where $\mathbf{u}$ is the velocity vector, p the fluid pressure, ρ the blood density, μ the dynamic viscosity of the fluid. Blood has been assumed to behave as shear thinning fluid and it has been modelled

using Bird-Carreau constitutive law

$$\mu_{app} = \mu_\infty + (\mu_0 - \mu_\infty)\left(1 + (\lambda s)^2\right)^{\frac{n-1}{2}}$$

where s is the blood shear rate and $\mu_\infty = 0.0035 kg\, m^{-1}\, s^{-1}$, $\mu_0 = 0.25 kg\, m^{-1}\, s^{-1}$, $\lambda = 25s$, n=0.25 [37]. The Bird-Carreau fluid model has proved to be suitable to display the fluid dynamic patterns within detailed geometries, especially those in near-wall zones and those of interest in terms of neointimal growth, as represented in a clipped stented coronary model in [27]. Blood density is $\rho = 1060\, kg\, m^{-3}$. The surface of the artery has been decomposed in several regions to impose boundary and interface conditions. Fully developed parabolic flow has been specified at the lumen inlet, $\Gamma_{l,in}$, no-slip condition has been applied at the vessel wall and on the stent $\Gamma_{end} \cup \Gamma_{stent}$ and the flow resistance at the outlet $\Gamma_{l,out}$ has been neglected,

$$\begin{aligned} \mathbf{u}(r) &= 2V_{med}\big(1 - (r/R)^2\big)\mathbf{k} && \forall \mathbf{x} \in \Gamma_{l,in} \\ p &= 0 && \forall \mathbf{x} \in \Gamma_{l,out} \\ \mathbf{u} &= \mathbf{0} && \forall \mathbf{x} \in \Gamma_{end} \cup \Gamma_{stent} \end{aligned}$$

The velocity data used in this work have been obtained from a prior study conducted on porcine coronary arteries [21]. The mean velocity values have been calculated by first extracting the experimental data values from [21] on a single cardiac cycle for the porcine right coronary artery and using these values to calculate the blood volume flow rate. The mean velocity for individual cases was obtained by fitting the flow with the measured angiographic diameter from the current experimental data. The peak velocity has been obtained through application of the integral mean value theorem on the inlet. A fully developed parabolic velocity profile is justified due to the distance from the aortic ostia, at which location plug flow would have been necessary, and its location upstream from the coronary ramifications, which would have incurred a reduction or redistribution of the blood flow.

The arterial wall geometry and stent are considered to be a rigid body with no-slip condition applied between the viscous fluid and the solid. While the actual coronary vasculature is known to contract and twist with the cardiac cycle, this boundary condition is justifiable due to the rigid nature that the stent imposes on the vascular wall [23]. In addition, the aim of this work is to focus on the fluid dynamics independently of the artery wall characteristics. Therefore, to accomplish this, the velocity of the hematic fluid at the wall is set to zero (no slip condition).

The blood flow is characterized by the Reynolds and Dean numbers:

$$Re = \frac{2\rho V_{med} R}{\mu_\infty}, \quad De = Re\sqrt{\delta} \tag{1}$$

According to the data used in this work, the magnitude of the Reynolds number, $Re = 106$, falls in the physiological range and the assumption of laminar flow is completely justified. The simulated curvature of the vessels leads in both cases (36 and 20 mm radii) to significant Dean numbers, respectively equal to 20.90 and 28.04 for the 36 mm and the 20 mm radii of curvature. According to the theory of curved pipes (see [16] for an application to arteries) we expect that curvature has non-negligible effects of on the flow and on the transported oxygen concentration.

Oxygen is carried in the blood flow as free oxygen dissolved in plasma and bounded to haemoglobin within red cells. We assume that the red blood cell concentration and the haemoglobin saturation are constant. Furthermore, since the transfer rate from free to bounded oxygen is much faster than the oxygen to wall transfer [25, 38], free and bound oxygen are at equilibrium in the blood stream. Then, given the concentration of dissolved oxygen into plasma, c, Henry's law can be used to explicitly obtain the oxygen partial pressure, which in turn determines the

hemoglobin saturation level and the concentration of bounded oxygen. In other words, determining the dissolved oxygen concentration is sufficient to completely characterize the total level of oxygen in blood as well as the transfer of oxygen to the arterial wall. Hence, following the lines of [34, 25, 33, 32] oxygen has been modeled using an advection-diffusion equation coupled to blood flow:

$$\nabla\cdot(-D_l\nabla c_l + \mathbf{u}c_l) = 0 \qquad \forall \mathbf{x} \in \Omega_l \tag{2}$$

where c_l is the dimensionless oxygen concentration with respect to the fully saturated oxygen level $c_0 = 0.0025\, ml_{0_2}/ml_{blood}$ (corresponding to oxygen partial pressure of 100 mmHg with a solubility constant of $2.5\cdot 10^{-5}\, ml_{0_2}/(ml_{blood}\cdot mmHg)$ [25]) and $D_l = 1.2\,10^{-9} m^2\, s^{-1}$ is the diffusivity of oxygen in blood [11, 25]. The artery wall has been assumed to be a single layer of solid material with the physical properties of the water (density of $1000\, kg\, m^{-3}$). Convective transport of oxygen within the wall tissue has been neglected since transmural velocities are significantly smaller than oxygen diffusion velocities [25]. Thus, wall-side oxygen transfer is given as:

$$\nabla\cdot(D_w\nabla c_w) + \sigma\, c_w = 0 \qquad \forall \mathbf{x} \in \Omega_w \tag{3}$$

where c_w is the dimensionless oxygen concentration in wall, $D_w = 0.9\,10^{-9} m^2\, s^{-1}$ is the diffusivity of oxygen in arterial wall [25] and $\sigma = 2.1\,10^{-5}\, ml_{0_2}/(ml\cdot s)$ [25] is a first order Michaelis-Menten reaction term has been introduced in order to take into account oxygen consumption by cells within the arterial tissue. At the lumen inlet, $\Gamma_{l,in}$, we impose a uniform concentration value of oxygen $c_l = 1$, while at the outlet, $\Gamma_{l,out}$ we apply an homogeneous Neumann condition $\nabla c_l \cdot \mathbf{n} = 0$. At the outer surface of the wall (adventitial surface, Γ_{adv}), the value of oxygen concentration is set to $c_w = 0.5$. In fact, experimental studies showed that the level of adventitial oxygen tension is about one half of the oxygen tension in blood [2]. It is reasonable to assume that oxygen does not chemically interact with the stent, thus we set $\nabla c_l \cdot \mathbf{n} = \nabla c_w \cdot \mathbf{n} = 0$ on Γ_{stent}. The matching conditions at the interface between fluid domain and artery wall enforce the continuity of both oxygen concentration and oxygen flux:

$$c_l = c_w \quad \text{and} \quad -D_l\nabla c_l\cdot\mathbf{n} = -D_w\nabla c_w\cdot\mathbf{n} \quad \forall \mathbf{x} \in \Gamma_{end}. \tag{4}$$

We observe that these conditions do not account for the endothelial barrier opposed to mass transfer. Our choice is motivated by the fact that the endothelium gets damaged during angioplastic procedures. More precisely, catheterization, balloon expansion and stenting can severely injure the endothelial integrity. It seems thus reasonable to neglect the presence of the endothelial layer, at least in the first days after the intervention. Oxygen transport in the lumen is characterized by the Péclét number

$$Pe_l = \frac{2V_{med}R}{D_l}$$

which is $Pe = 290\dot{}766$ and shows that the dynamics of oxygen in the lumen is, as expected [25], highly transport dominated. For this reason, special attention in the discretization of this equation is required, as discussed below. For the oxygen transport within the artery, the diffusion / reaction equation is characterized by the Damkohler number

$$Da = \frac{\sigma r h}{D_w c_0}.$$

The reported data on the oxygen absorption coefficient in the wall of healthy arteries are rare and highly variable [25, 2, 13, 40, 38, 31]. The Damkohler number obtained here is $Da = 1.33$, computed on the basis of fully saturated oxygen level $c_0 = 0.0025\, ml_{0_2}/ml_{blood}$. Nonetheless, due to the uncertainty in literature about oxygen reaction kinetics in the artery, we have tested different values of the oxygen consumption coefficient, σ, within the range from 0.0021 $ml_{0_2}/(ml_{tissue}\cdot s)$ to 0.000021 $ml_{0_2}/(ml_{tissue}\cdot s)$ obtaining negligible differences in oxygen patterns.

2.4 Computational methods

To carry out the fluid dynamic and mass transport simulations, we have used the commercial code ANSYS CFX v.13.0 (Ansys Inc., Canonsburg, PA, USA). The spatial discretization is based on a cell based finite volume method [39]. More precisely, the Laplace operator in the fluid momentum and oxygen transport equations is approximated by a centered scheme, while the convective terms have been discretized by means of an upwind method. The convective term in the Navier-Stokes equations is linearized by means of Picard iterations (equivalent to a *fictitious* time stepping method with semi implicit treatment of $\mathbf{u} \cdot \nabla \mathbf{u}$) ("ANSYS CFX-Solver Theory Guide", ANSYS Inc., 2010). The pressure variable in the Navier-Stokes equations is evaluated at the same nodes of the velocity field and a *coupled* (i.e. monolithic) strategy is adopted for the assembly and solution of the linear system of equations. The system is finally solved using an algebraic multigrid method exploiting incomplete LU factorization as smoother. Numerical simulation have been preformed on parallel CPUs using a 2 Quad-Core Intel Xeon processors, 8 GB RAM at the Politecnico di Milano and a quad-socket 12-Core AMD Magny Cours CPU, 128 GB RAM at University of Pittsburgh. Convergence criteria were set to 10^{-6} for the normalized residuals of the global linear system of equations.

The final meshes features 16˙139˙357, 22˙875˙422, 15˙909˙987 elements, and 2˙668˙336, 3˙782˙312, 2˙631˙468 nodes for the straight and curved vessels (with curvature radii 20 and 36 mm respectively). Grid sensitivity analysis has been performed, starting from a coarse mesh featuring 3˙810˙591 elements. The numerical solution on a coarse mesh has been compared with the ones obtained on meshes counting 3 and 6 times more elements. We selected the absolute maximum and minimum of oxygen concentration inside the arterial walls as indicators of grid independence. The maximum of oxygen concentration varies of 15% with the first refinement and 5% for the second. The minimum changed of 1.3% with the first refinement and 0.1% for the second. Our conclusion is that the intermediate refinement level is accurate enough to capture the significant characteristics of oxygen concentration profiles.

3 Results

The analysis of perturbed blood flow in presence of stents has been investigated by several studies [29, 28]. The present work aims to complement the existing literature with the investigation of the following points: (i) the role of vessel curvature on flow and WSS patterns; (ii) the combined analysis of blood flow and oxygen transfer.

3.1 Hemodynamics

The flow patterns for different values of the vessel curvature are reported in Figure 2. For the curved vessels, as expected, the velocity peak is shifted towards the *outer* surface of the wall, with respect to the center of curvature.

In order to quantify secondary flows on selected cross sections of the model, the helicity is addressed. By definition, the helicity of an infinitesimal portion of fluid is defined as the scalar product of the velocity and the vorticity fields [8, 17], namely $(\nabla \times \mathbf{u}) \cdot \mathbf{u}$, and consequently it measures the alignment of the velocity and vorticity vectors. Positive values of helicity correspond to a clockwise rotation of the flow, and negative values to a counter clockwise rotation. In-plane velocity vectors with uniform length are also superimposed to helicity contours to better visualize the secondary flows, see Figure 3. We notice that secondary flows are present in all the cases, also in the straight vessel model. However significant secondary flows only appear in the two curved models, with peaks of helicity values grater than 10 $m\,s^{-2}$.

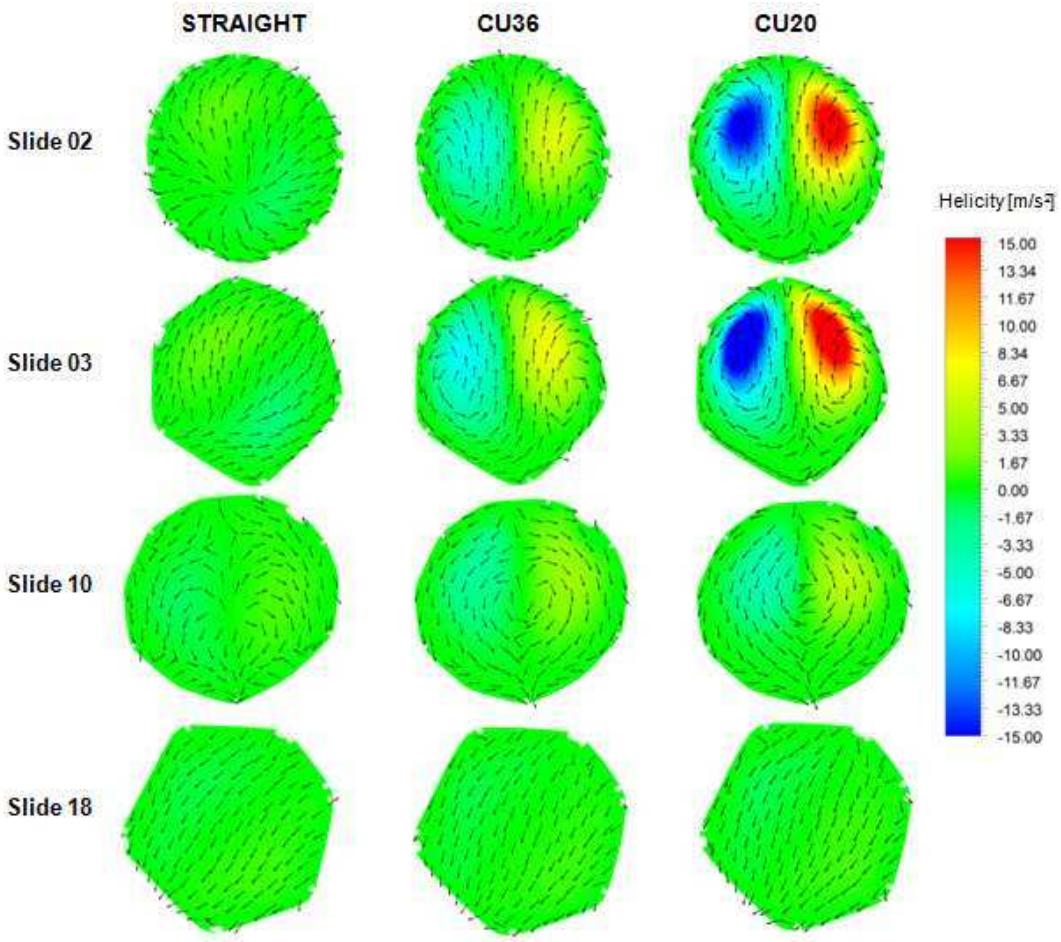

Figure 3: Helicity contours with in-plane velocity vectors at selected cross sections. Even if secondary flows are present in all the cases, they become significant only in the two curved models, with peaks of helicity values grater than 10 $m\,s^{-2}$. Positive values of helicity correspond to a clockwise rotation of the flow, and negative values to a counter clockwise rotation.

These flow perturbations directly affect the WSS profiles at the interface between the lumen and the wall. In Figure 4 we compare for different vessel curvatures the WSS patterns observed from the top side of the lumen (*outer* surface with respect to the center of curvature), from the bottom side (or *inner* surface) and from the *lateral* viewpoint. Significant differences are observed, confirming that the curvature induced flow perturbations affect the bio-mechanical conditions of the artery.

3.2 Mass transfer

The general inspection of the oxygen concentration plotted on the luminal interface of the artery, Figure 5, illustrates that the stent struts perturb the oxygen distribution. More precisely, oxygen concentration lower than the bulk value is systematically observed in the vicinity of the stent. This effect is also clearly visible in the sequence of Figures 7, 8, 9, where the location of the stent struts (top) is quantitatively compared with the local minima of oxygen concentration (middle panel) and WSS (bottom panel). In addition, for the curved models in Figure 5, a greater area of low oxygen concentration appears at the inner side of the endothelial surface,

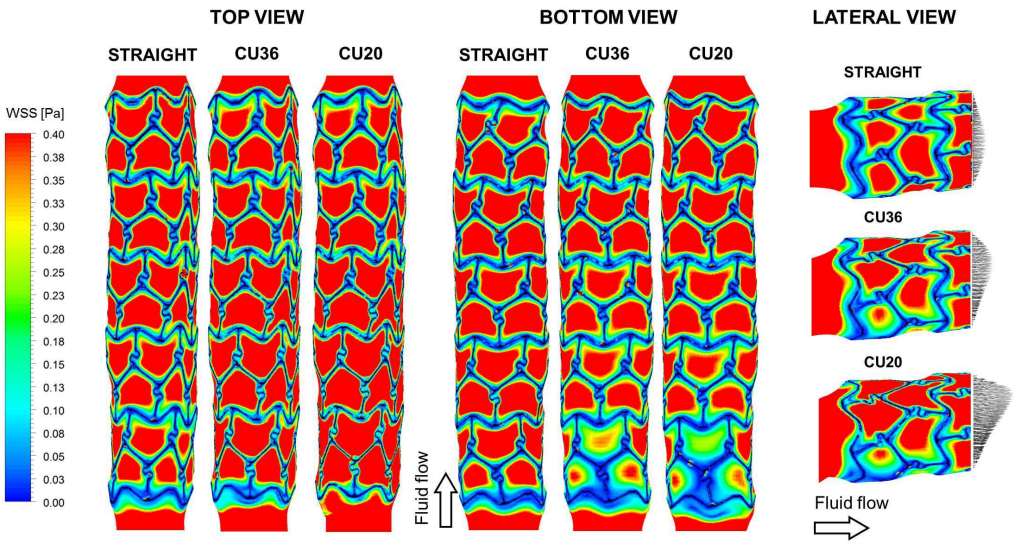

Figure 4: Comparison of the WSS contour maps for the three considered geometries: straight, CU36 (36 mm radius of curvature), and CU20 (20 mm radius of curvature). From left to right, the top, bottom and lateral views are displayed. Minimum values of WSS occur at the inlet of the stented region. This effect is prominent for CU36 and CU20 cases, due to the curvature.

with a minimum near the inlet of the stented region.

The comparison of Figures 4 and 5 highlights that the WSS and oxygen surface patterns are not completely equivalent. More precisely, while the main region of low WSS is confined nearby the inlet, the perturbation of oxygen concentration extends along the entire length of the artery. This effect corresponds to a thickening of the concentration boundary layer, which could be promoted by both the vessel curvature and the sequential combination of strut wakes.

To further analyze the combined effects of flow and transport, it is also interesting to compare the concentration contours on selected cross sections, with the visualization of the secondary flows on the same sectional planes (see Figure 3 and 6 respectively). Counter rotating Dean vortexes are clearly visible in all cases, but their strength increases with the curvature of the vessel. Similarly to what has been observed in the results presented in [31], the interaction of these vortexes with mass transfer gives origin to an area of reduced oxygen concentration that is visibly evident in Figure 6. These results match with the recent literature in the assessment that the geometry-modified distribution of WSS creates a region of lower oxygen flux along the inner curved wall [12, 11].

4 Discussion

4.1 Inspection of the arterial histologies at different axial locations

Figure 1 shows the histologies at different sections spanning the entire stented region of the porcine coronary artery harvested from the animal study addressed in section 2.1. We are particularly interested to examine the presence and the extension of ISR, that is typically the consequence of neointimal hyperplasia. ISR appears at several locations throughout the arterial axis. In particular, only for slides 4 and 6 ISR seems to be almost negligible, while for the remaining sections a significant remodelling of the intimal layer takes place. On the basis of these data, we highlight the following observations. Firstly, a major arterial stenosis is visible in section 2. Secondly, ISR is more prominent at the *bottom* part of the vessel (with respect to

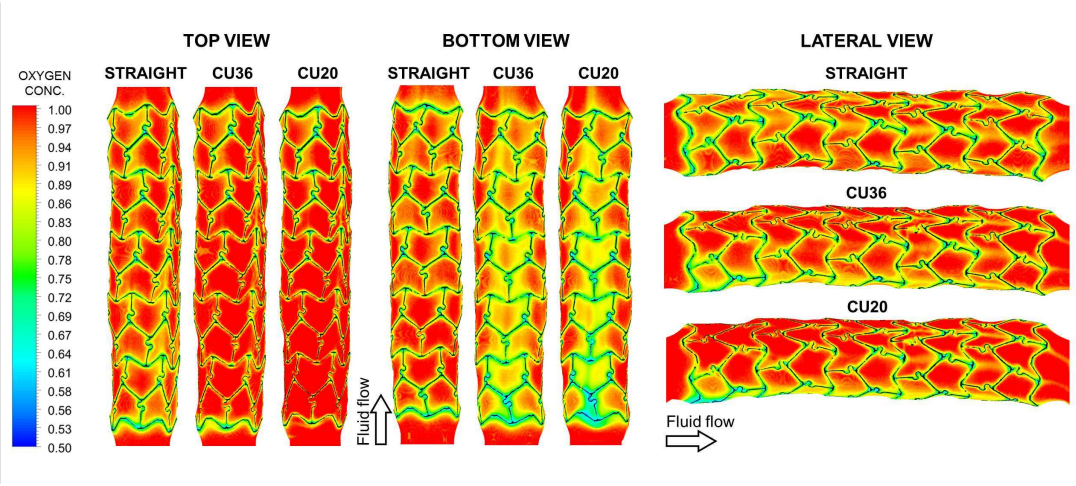

Figure 5: Oxygen concentration contour maps for the three considered geometries: straight, CU36 (36 mm radius of curvature), and CU20 (20 mm radius of curvature). From left to right, the top, bottom and lateral views are displayed. Minimum values of oxygen concentration are located close to the stent struts and, in particular, next to the strut links. The vessel curvature strongly affects the oxygen distribution near the wall.

the visualized orientation). According to the geometrical reconstruction, it corresponds to the *inner* region of the artery with respect to the heart. ISR involves complex remodelling phenomena caused by the superposition of multiple different factors such as hemodynamic forces on the endothelial layer, non physiological stresses in the arterial wall, injuries caused by stent deployment, etc. All of these quantities do not provide absolute certainty of the emergence of ISR, but only increase the risk and predisposition of the arterial wall to experience ISR. The determination of the precise role of each factor on ISR is a challenge even using the most advanced computational models. For this reason, we restrict our objective to establishing a correlation between the geometry of the vessel, the perturbations of WSS and oxygen concentrations, and the observation of significant ISR.

4.2 The role of geometry on blood flow patterns

We identify two main features that characterize this vascular district; (i) the presence of an abrupt variation of the vessel diameter, due to the implantation of the stent, and (ii) the curvature of the arterial segments proximal and distal to the stent. It is widely accepted that perturbations of homoeostatic shear stress affect vascular remodelling and pathobiology. According to Malek *et al.* [24] WSS around (or below) 0.4 Pa are typical of those regions susceptible to develop atherosclerotic disease. A thorough description of the correlation between hemodynamic forces and ISR is available in [27] for the straight vessel model investigated in this work. The analysis of figures 4, 3 suggests that the flow perturbation induced by the variation in diameter is confined to the first ring of the stent, while the shifting from straight to curved vessels affects the entire flow field, as expected from the analysis of Dean numbers. The most significant differences between straight and curved models are located at the proximal entrance of the stented region; in particular, a wider area of low WSS is observed at the inner surface of the endothelium, in correspondence to fluid flow recirculation, stasis and flow separation regions. By combining these simulations with the observation of histologies, we infer that the significant stenosis at the proximal section of the artery is likely to be related to the transition

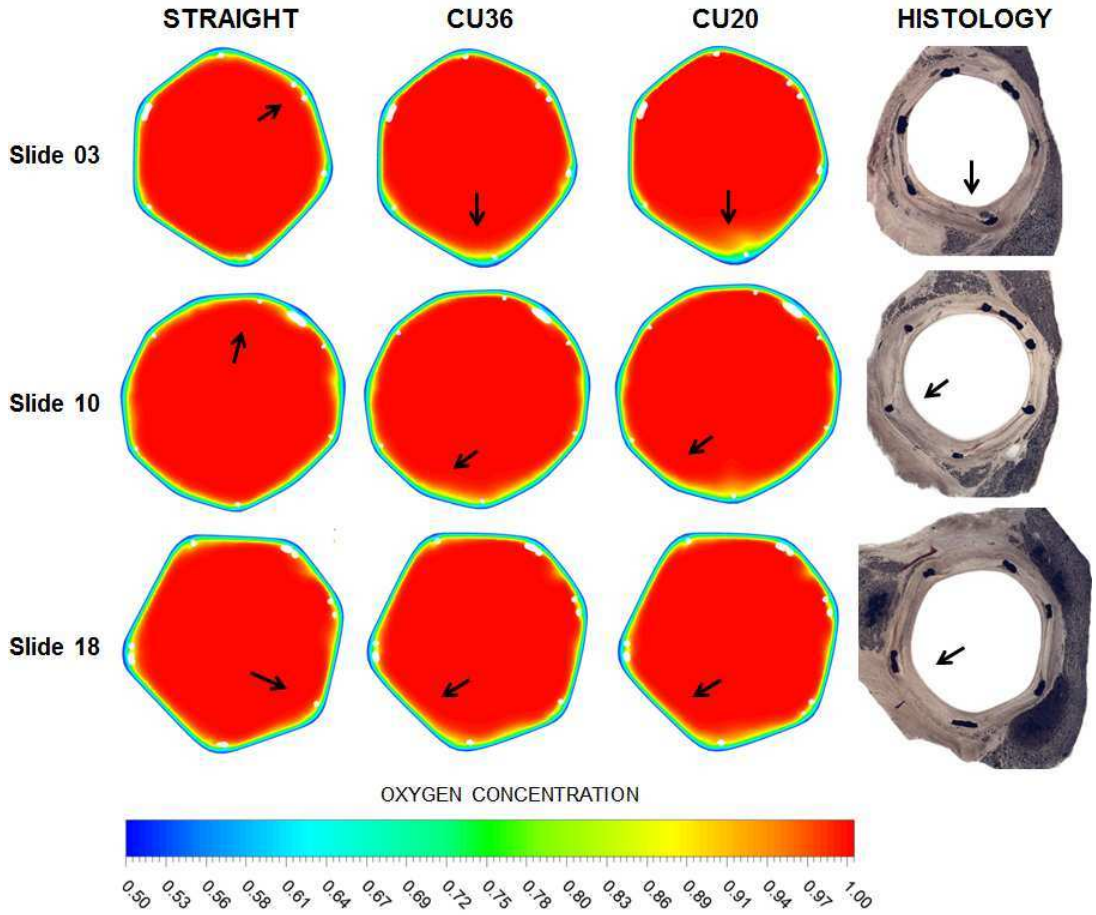

Figure 6: Qualitative comparison of the oxygen concentration between the computational models (straight, CU36, CU20) and the corresponding histological images at three selected sections. Black arrows indicate the wall region with lowest oxygen concentration in the computational models and greatest neointimal thickness in the histologies. From a qualitative point view, a correlation between the oxygen concentration and the neointimal thickness can be observed in the case of the curved models.

between the untreated and stented portions of the artery. Given the irregular WSS patterns in the central and distal portions of the artery, it is more difficult to directly attribute the onset of ISR to flow perturbations.

4.3 Analysis of oxygen patterns and the effect of hypoxia on in-stent restenosis

We can not examine oxygen concentration *in vivo*, because the current oxygen measurement techniques were not performed in the present animal data set. The findings from literature identify greater amounts of neointimal thickening with lowered oxygen conditions, namely below 30 mmHg (e.g. pimonidazole injection [6], oxygen tension probe [36]), while hypoxia exists in conditions where the P_{O_2} levels are below 10 mmHg [36, 7].

The inner regions of the stented model within the study are subjected to lower oxygen flux, as shown in Figure 5 (bottom view), in particular for the curved configurations. In Figure 6 a comparison between the computational results (oxygen concentration) and the corresponding histological observations is shown. The displayed arrows point at sites of prominent ISR (histological images) and at the wall regions subjected to the lower oxygen concentration (computational results). For the highest curvature levels, there is a good correspondence between these locations and extended regions affected by low oxygen supply. These findings suggest that the presence of extended ISR on the bottom surface of the wall correlates better with low oxygen concentration that to low WSS. For the straight model the correlation between lower oxygen concentration and higher neointimal thickness is not observed; this may be due to the simplification adopted while modelling a straight model with is not consistent with histological observations.

Quantitatively, the minimum blood oxygen concentration reaches 47.6% of the bulk value for the straight model, while 48.2% and 44.3% of the bulk values have been calculated for the 36 mm and 20 mm radius of curvature models respectively. Even though these concentration levels are not low enough to speak of hypoxia, in all cases the minimum oxygen concentration is barely half of the bulk value. A more quantitative evidence of how the combination of perturbed flow, low WSS and persistently reduced oxygen supply affects ISR, is displayed in figures 7, 8, 9, for increasing values of the curvature radius. Therefore, for different arterial cross sections, we plot the profile of WSS and oxygen concentration along the perimeter of the luminal surface. The inspection of histologies allows us to compare the variation of such quantities with the amount to arterial regrowth. We notice that at locations $-120^o < \theta < -80^o$ for slide 3, $-120^o < \theta < -90^o$ for slide 10 and $\theta \simeq -100^o$ for slide 18, extended regions of reduced WSS and oxygen concentration closely correspond to significant ISR.

In conclusion, a persistent state of such a low oxygenation could likely affect the arterial homeostasis. As the oxygen supply along the luminal tissue of arteries has been considered critical for the metabolic needs of the intima and inner one-third of the artery, as the outer two thirds are supplied by the *vasa vasorum*, the inner media is constantly on the verge of hypoxia and therefore might be expected to be very sensitive to alterations in oxygen tension and intimal thickness [9]. The local hemodynamic changes could also result in reduced transport of metabolites [9]. While the results only show a weak indication of hypoxia, the lower oxygen trend does indicate that this response may play some role in the tissue healing process.

4.4 Limitations

At the level of simulations, the main limitation of this work rests on the approximation of blood flow with a steady model for rigid arteries, which is substantially motivated by the need to limit the yet considerable computational cost of the entire model. Because of the peculiarity

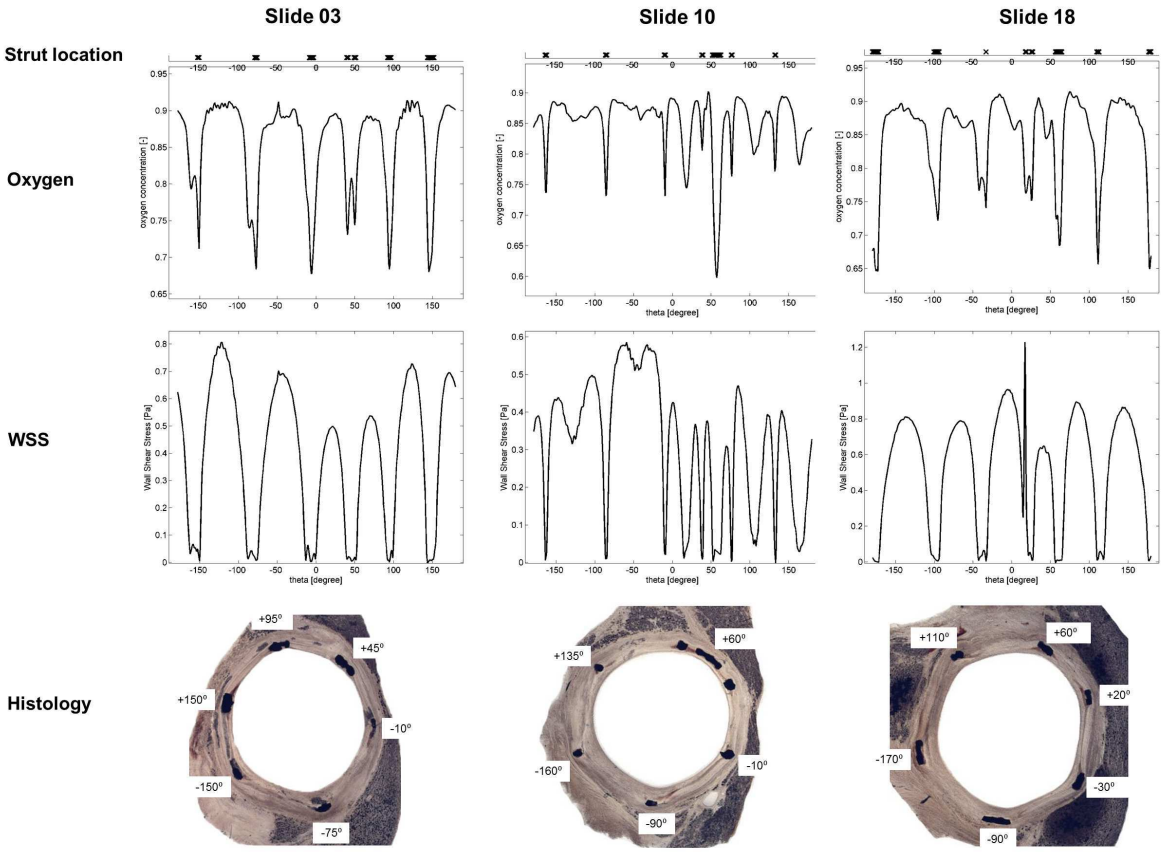

Figure 7: Quantitative comparison of oxygen concentration and WSS with ISR for three cross sections of the straight arterial model.

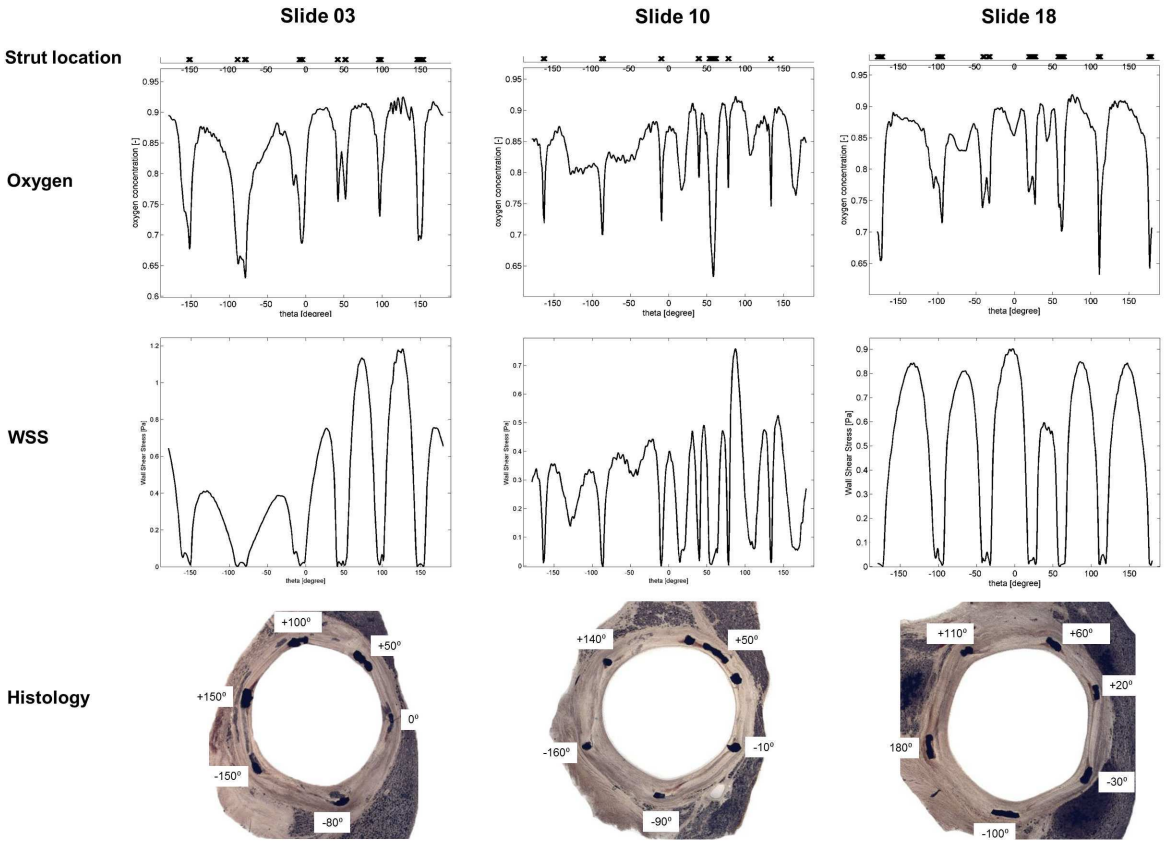

Figure 8: Quantitative comparison of oxygen concentration and WSS with ISR for three cross sections of the CU36 (36 mm radius) arterial model.

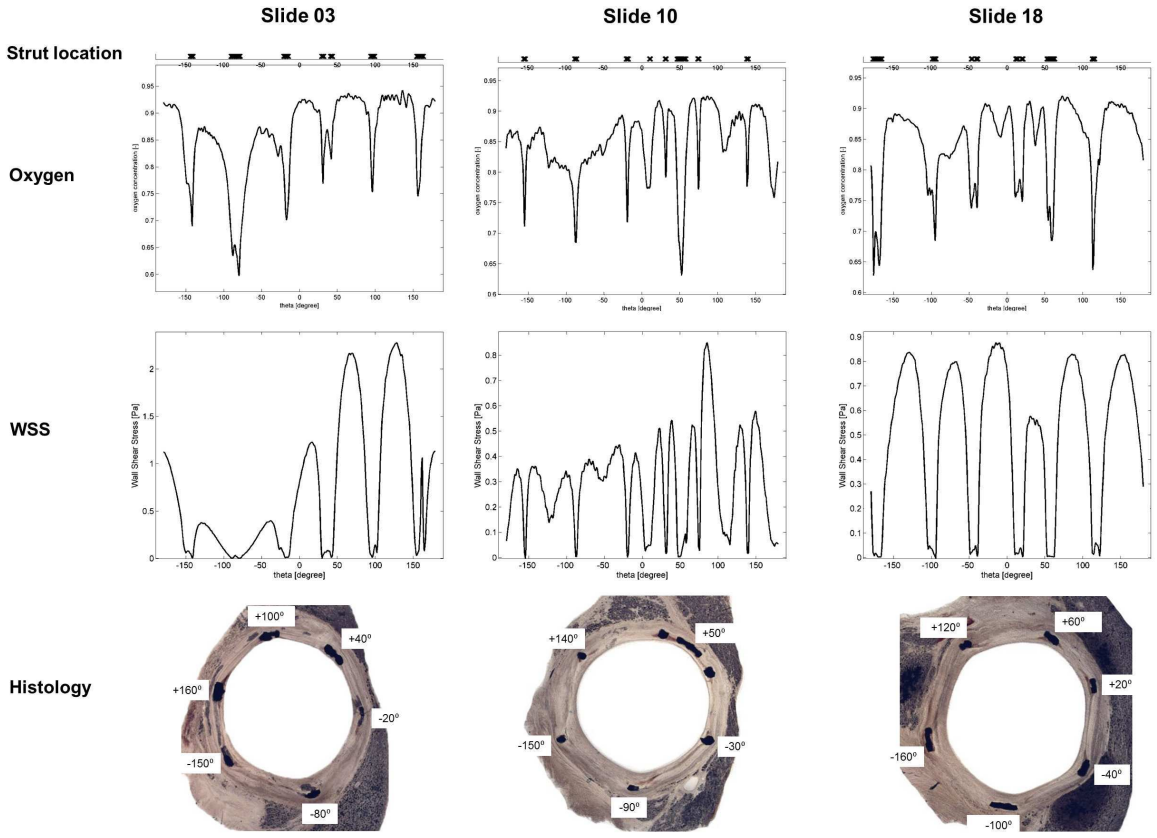

Figure 9: Quantitative comparison of oxygen concentration and WSS with ISR for three cross sections of the CU20 (20 mm radius) arterial model.

of hemodynamic conditions characterizing coronary arteries, it is difficult to address this issue without exceeding in the complexity of the model. On one hand, it is well known that the flow profile in coronary arteries does not match with the classical systolic / diastolic waveform of the systemic tree [19]. Furthermore, not only the pulsation, but also the heart contraction affects the blood flow profiles. On the other hand, the interaction of hemodynamics and arterial wall remodelling is usually related to averaged indicators over the heart cycle, such as the time averaged WSS, see as an example [1, 3, 5]. For these reasons, we believe that the steady flow and transport models represent a reasonable trade-off between computational cost and model accuracy.

The quality and quantity of available biological data could also be improved. The addition of biplane angiography would provide the real coronary centerline. From a biological standpoint, using other imaging modalities would help to reconstruct not only the stent but also the vessel geometry. These data could be gathered through optical coherence tomography (OCT), intravascular ultrasound (IVUS), or optical projection tomography (OPT). In this study we have focused our attention on the methodology to compare in silico with in vivo observations. The natural evolution of this analysis consists in extending the present investigation form a single experimental animal case to more cases, as more samples are needed for more reliable inferences.

5 Conclusions

The development of neointimal hyperplasia and, as a consequence, of the in-stent restenosis leads to the failure of the stent. The causes determining the initiation of such pathologies are still unclear. Several literature studies highlighted a correlation between abnormal local flow field, in particular wall shear stresses distribution and ISR [3, 4]. Moreover, a relation between hypoxia and ISR may exist [36, 11, 12]. Indeed the hypoxia leads to an increase in the endothelium permeability to lipids, to the activation of the macrophages and to the adhesion of the proteins. In this work we aimed at analyzing the influence of geometrical factors, WSS and low oxygen concentration on neointimal hyperplasia in a stented porcine coronary artery. Among geometrical factors we account for the vessel curvature. For this reason, we have compared three different geometries of the stented artery i.e., a straight model, CU36 model (36 mm radius of curvature) and CU20 model (20 mm radius of curvature). The comparison of these computational results with the histological observations gives rise to important considerations. The histological observation showed that a major arterial stenosis is visible at the inlet of the stented region and in particular in the inner (or bottom) side of the vessel. This evidence is corroborated by the computational findings. In this region, the widest area with low WSS and low oxygen concentration was found. Moreover, as the curvature increases, the most critical condition (i.e., low WSS and low oxygen concentration) occurs at the inner side of the arterial wall. This phenomenon is due to flow recirculation, stasis and separation regions, which is more evident in the curved models. Finally, for all the three geometries, the presence of the stent significantly alters the local fluid dynamics and the mass transfer. All of these considerations highlight the difficulties in the understanding of complex biological phenomena such as the ISR development. Nevertheless, this work can provide preliminary indications on the regions that may be more susceptible to the ISR by accounting for the principal actors involved in this phenomenon.

References

[1] T. Asakura and T. Karino. Flow patterns and spatial distributions of atherosclerotic lesions in human coronary arteries. *Circulation Research*, 66(4):1045–1066, 1990.

[2] D.G. Buerk and T.K. Goldstick. Arterial wall oxygen consumption rate varies spatially. *Am. J. Physiol. Heart Circ. Physiol*, 243:948958, 1982.

[3] C.G. Caro, J.M. Fitz-Gerald, and R.C. Schroter. Arterial wall shear and distribution of early atheroma in man [18]. *Nature*, 223(5211):1159–1161, 1969.

[4] C.G. Caro, J.M. Fitz-Gerald, and R.C. Schroter. Atheroma and arterial wall shear observation, correlation and proposal of a shear dependent mass transfer mechanism for atherogenesis. *Proceedings of the Royal Society of London. Series B. Biological Sciences*, 177:109–133, 1971.

[5] L.-J. Chang and J.M. Tarbell. A numerical study of flow in curved tubes simulating coronary arteries. *Journal of Biomechanics*, 21(11):927–937, 1988.

[6] A.N. Cheema, T. Hong, N. Nili, A. Segev, J.G. Moffat, K.E. Lipson, A.R. Howlett, D.W. Holdsworth, M.J. Cole, B. Qiang, F.Kolodgie, R. Virmani, D.J. Stewart, and B.H. Strauss. Adventitial microvessel formation after coronary stenting and the effects of su11218, a tyrosine kinase inhibitor. *Journal of American College of Cardiology*, 47:1067–1075, 2006.

[7] A.N. Cheema, T. Hong, N. Nili, A. Segev, J.G. Moffat, K.E. Lipson, A.R. Howlett, D.W. Holdsworth, M.J. Cole, B. Qiang, F. Kolodgie, R. Virmani, D.J. Stewart, and B.H. Strauss. Adventitial microvessel formation after coronary stenting and the effects of su11218, a tyrosine kinase inhibitor. *Journal of the American College of Cardiology*, 47(5):1067–1075, 2006.

[8] C. Chiastra, S. Morlacchi, S. Pereira, G. Dubini, and F. Migliavacca. Computational fluid dynamics of stented coronary bifurcations studied with a hybrid discretization method. *European Journal of Mechanics B/Fluids*, 35:76–84, 2012.

[9] G.M. Chisolm, J.L. Gainer, G.E. Stoner, and J.V.Jr. Gainer. Plasma proteins, oxygen transport and atherosclerosis. *Atherosclerosis*, 15:327–343, 1972.

[10] J.J. Chiu and S. Chien. Effects of disturbed flow on vascular endothelium: Pathophysiological basis and clinical perspectives. *Physiological Reviews*, 91:327–387, 2011.

[11] G. Coppola and C. Caro. Oxygen mass transfer in a model three-dimensional artery. *J. R. Soc. Interface*, 5:10671075, 2008.

[12] G. Coppola and C. Caro. Arterial geometry, flow pattern, wall shear and mass transport: potential physiological significance. *J. R. Soc. Interface*, 6:519528, 2009.

[13] D.W. Crawford and D.H. Blankenhorn. Arterial wall oxygenation, oxyradicals, and atherosclerosis. *Atherosclerosis*, 89:97108, 1991.

[14] E. Cutrì, P. Zunino, S. Morlacchi, C. Chiastra, and F. Migliavacca. Drug delivery patterns for different stenting techniques in coronary bifurcations: a comparative computational study. *Biomech Model Mechanobiol*, DOI 10.1007/s10237-012-0432-5, 2012.

[15] P.F. Davies. Flow-mediated endothelial mechanotransduction. *Physiological Reviews*, 75:519–560, 1995.

[16] Denis Doorly and Spencer Sherwin. Geometry and flow. In *Cardiovascular mathematics*, volume 1 of *MS&A. Model. Simul. Appl.*, pages 177–209. Springer Italia, Milan, 2009.

[17] D. Gallo, D.A. Steinman, P.B. Bijari, and U. Morbiducci. Helical flow in carotid bifurcation as surrogate marker of exposure to disturbed shear. *Journal of Biomechanics*, 45:23982404, 2012. DOI: 10.1016/j.jbiomech.2012.07.007.

[18] D. Gastaldi, S. Morlacchi, R. Nichetti, C. Capelli, G. Dubini, L. Petrini, and F. Migliavacca. Modelling of the provisional side-branch stenting approach for the treatment of atherosclerotic coronary bifurcations: effects of stent positioning. *Biomech Model Mechanobiol.*, 9:551–561, 2010.

[19] X. He and D.N. Ku. Pulsatile flow in the human left coronary artery bifurcation: Average conditions. *Journal of Biomechanical Engineering*, 118(1):74–82, 1996.

[20] W.C. Heuper. Arteriosclerosis. the anoxemia theory. *Archives of Pathology*, 39:245–350, 1944.

[21] Y. Huo, J.S. Choy, M. Svendsen, A.K. Sinha, and G.S. Kassab. Effects of vessel compliance on flow pattern in porcine epicardial right coronary arterial tree. *Journal of Biomechanics*, 42:594602, 2009.

[22] J.F.Jr. LaDisa, L.E. Olson, I. Guler, D.A. Hettrick, S.H. Audi, J.R. Kersten, D.C. Warltier, and P.S. Pagel. Stent design properties and deployment ratio influence indexes of wall shear stress: a three-dimensional computational fluid dynamics investigation within a normal artery. *J. Appl. Physiol.*, 97:424–430, 2004.

[23] J.F. LaDisa Jr., D.A. Hettrick, L.E. Olson, I. Guler, E.R. Gross, T.T. Kress, J.R. Kersten, D.C. Warltier, and P.S. Pagel. Stent implantation alters coronary artery hemodynamics and wall shear stress during maximal vasodilation. *Journal of Applied Physiology*, 93(6):1939–1946, 2002.

[24] A.M. Malek, S.L. Alper, and S. Izumo. Hemodynamic shear stress and its role in atherosclerosis. *J.Am.Med.Assoc.*, 282:2035–2042, 1999.

[25] J.A. Moore and C.R. Ethier. Oxygen mass transfer calculations in large arteries. *Journal of Biomechanical Engineering*, 119:469–475, 1997.

[26] S. Morlacchi, C. Chiastra, D. Gastaldi, G. Pennati, G. Dubini, and F. Migliavacca. Sequential structural and fluid dynamic numerical simulations of a stented bifurcated coronary artery. *Journal of Biomechanical Engineering*, 133:1–11, 2011.

[27] S. Morlacchi, B. Keller, P. Arcangeli, M. Balzan, F. Migliavacca, G. Dubini, J. Gunn, N. Arnold, A. Narracott, D. Evans, and P. Lawford. Hemodynamics and in-stent restenosis: Micro-ct images, histology, and computer simulations. *Annals of Biomedical Engineering*, 2011. DOI: 10.1007/s10439-011-0355-9.

[28] S. Morlacchi and F. Migliavacca. Modeling stented coronary arteries: Where we are, where to go. *Ann Biomed Eng.*, Article in Press.:1–17, 2012. DOI: 10.1007/s10439-012-0681-6.

[29] J.B. Murphy and F.J. Boyle. Predicting neointimal hyperplasia in stented arteries using time-dependent computational fluid dynamics: a review. *Comput. Biol. Med.*, 40:408418, 2010. DOI: 10.1016/j.compbiomed.2010.02.005.

[30] W.W. Nichols and M.F. O'Rourke. *McDonald's Blood Flow in Arteries*. Lea and Febiger, Philadelphia, 3rd edition, 1990.

[31] Y. Qiu and J.M. Tarbell. Numerical simulation of oxygen mass transfer in a compliant curved tube model of a coronary artery. *Ann. Biomed. Eng.*, 28:26–38, 2000.

[32] A. Quarteroni, A. Veneziani, and P. Zunino. A domain decomposition method for advection-diffusion processes with application to blood solutes. *SIAM Journal on Scientific Computing*, 23(6):1959–1980, 2002.

[33] A. Quarteroni, A. Veneziani, and P. Zunino. Mathematical and numerical modeling of solute dynamics in blood flow and arterial walls. *SIAM Journal on Numerical Analysis*, 39(5):1488–1511, 2002.

[34] G. Rappitsch and K. Perktold. Computer simulation of convective diffusion processes in large arteries. *J. Biomech.*, 29:207–215, 1996.

[35] J.I. Sanada, O. Matsui, J. Yoshikawa, and T. Matsuoka. An experimental study of endovascular stenting with special reference to the effects on the aortic vasa vasorum. *Cardiovascular and Interventional Radiology*, 21:45–49, 1998.

[36] S.M. Santilli, A.S. Tretinyak, and E.S. Lee. Transarterial wall oxygen gradients at the deployment site of an intra-arterial stent in the rabbit. *Am J Physiol Heart Circ Physiol*, 279:1518–1525, 2000.

[37] T. Seo, L.G. Schachter, and A.I. Barakat. Computational study of fluid mechanical disturbance induced by endovascular stents. *Ann. Biomed. Eng.*, 33:444–456, 2005.

[38] S. Tada. Numerical study of oxygen transport in a carotid bifurcation. *Phys. Med. Biol.*, 55:3993–4010, 2010.

[39] H.K Versteeg and W. Malalasekera. *An introduction to computational fluid dynamics - The Finite Volume Method*. Longman Scientific and Technical, 1995.

[40] P. Zunino. *Mathematical and numerical modeling of mass transfer in the vascular system*. PhD thesis, École Polytechnique Fédérale de Lausanne, 2002.

[41] P. Zunino, C. DAngelo, L. Petrini, C. Vergara, C. Capelli, and F. Migliavacca. Numerical simulation of drug eluting coronary stents: Mechanics, fluid dynamics and drug release. *Comput. Methods Appl. Mech. Engrg.*, 198:36333644, 2009.

MOX Technical Reports, last issues

Dipartimento di Matematica "F. Brioschi",
Politecnico di Milano, Via Bonardi 9 - 20133 Milano (Italy)

05/2013 Caputo, M.; Chiastra, C.; Cianciolo, C.; Cutri , E.; Dubini, G.; Gunn, J.; Keller, B.; Zunino, P.;
Simulation of oxygen transfer in stented arteries and correlation with in-stent restenosis

04/2013 Morlacchi, S.; Chiastra, C.; Cutr, E.; Zunino, P.; Burzotta, F.; Formaggia, L.; Dubini, G.; Migliavacca, F.
Stent deformation, physical stress, and drug elution obtained with provisional stenting, conventional culotte and Tryton-based culotte to treat bifurcations: a virtual simulation study

03/2013 Antonietti, P.F.; Ayuso de Dios, B.; Bertoluzza, S.; Pennacchio, M.
Substructuring preconditioners for an $h-p$ Nitsche-type method

02/2013 Brugiapaglia, S.; Gemignani, L.
On the simultaneous refinement of the zeros of H-palindromic polynomials

01/2013 Arnold, D.N.; Boffi, D.; Bonizzoni,F.
Tensor product finite element differential forms and their approximation properties

56/2012 Ieva, F.; Paganoni, A.M.
Risk Prediction for Myocardial Infarction via Generalized Functional Regression Models

55/2012 Peng Chen, Alfio Quarteroni, Gianluigi Rozza
Uncertainty quantification of the human arterial network

54/2012 Ettinger, B., Perotto, S.; Sangalli, L.M.
Spatial regression models over two-dimensional manifolds

53/2012 Fumagalli, A.; Scotti, A.
An efficient XFEM approximation of Darcy flows in fractured porous media

52/2012 Perotto, S.
Hierarchical model (Hi-Mod) reduction in non-rectilinear domains